A Water Model Study of Impinging Gas Jets on Liquid Surfaces

HO YONG HWANG and GORDON A. IRONS

Water modeling experiments were designed to observe the deformation of a liquid surface by impinging the gas jet. Video images were taken and processed in a systematic way. The important surface cavity parameters, such as depth, width, and their frequency of oscillation, were obtained. The relation between surface depression depth and the supplied gas momentum were consistent with previous findings and were extended to higher flow rates. The surface instability and the onset of splashing were observed and interpreted with the Blowing number. The wave behaviors were described qualitatively with a combination of photographic evidence and power spectral density analysis to extract the characteristic wave numbers for each gas flow rate. The analysis of the time series of the surface variables showed a connection to the attenuation of turbulence gas pressure fluctuation and the surface deformation by the gas impingement. Bath velocities were measured with a particle image velocimetry (PIV) technique. To quantify the transfer of kinetic energy from the gas to the liquid, an energy transfer index was defined and calculated with the PIV data. The index was insensitive to gas flow rate but increased with cavity width. The momentum transfer across the interface was also analyzed, and a similar cavity width dependence was found. A correlation between the cavity shape and momentum transfer was proposed.

DOI: 10.1007/s11663-011-9613-3

I. INTRODUCTION

THE basic oxygen furnace (BOF) process uses supersonic oxygen jets that impinge on the metal bath surface, and the impingement process promotes the refining reactions and slag formation. The BOF has an extremely high refining rate partly because of the large amount of interfacial area created among the metal, slag, and gas phases by the high jet momentum; the metal and gas phases are considered to be emulsified in the slag layer.[1] The contribution of the extra area to the overall reaction rate is estimated to be less than 50 pct.[2] The other site for the high reaction rate is the hot spot at the jet impingement or impact point. The temperature measured by optical pyrometry around that impingement point is 2273 K to 2673 K (2000 °C to 2400 °C), which is 773 K to 1073 K (500 °C to 800 °C) higher than bulk bath temperature, and it is estimated that 75 to 80 pct of the carbon is removed in the jet impact zone.[2] Therefore, the effects of the oxygen jet are important for the determination of the following:

- The liquid cavity shape and area at the impingement point.
- Droplet formation and the subsequent droplet trajectory and residence time in the slag.[3]
- The transfer of momentum to provide stirring in the metal bath.

The current state of knowledge for each of these aspects will be reviewed briefly.

A. *Cavity Shape*

In principle, the cavity shape and area are a result of the combined effects of the dynamic pressure from the jet, gravity, and the capillary forces. Molloy[4] classified the response of the liquid surface to an impinging jet into dimpling, splashing, and penetrating stages; the classification criteria were based mainly the surface stability as a function of the gas impingement velocity.

Banks and Chandrasekhara[5] were the first investigators to develop a fundamental relationship between the momentum of a turbulent jet and the depth of penetration n_o. They combined a turbulent jet centerline velocity relationship[6] with a balance between gas dynamic pressure and buoyancy at the impact point to obtain the following dimensionless relationship:

$$\frac{\dot{M}}{\rho_l g h^3} = \frac{\pi}{2K^2}\frac{n_0}{h}\left(1+\frac{n_0}{h}\right)^2 \qquad [1]$$

An equivalent relationship was developed by Turkdogan.[7] Koria and Lange[8] extended the analysis to jetting from multiple holes. Qian *et al.*[9] modified Eq. [1] slightly and fitted $F_q = \dot{M}/\rho_l g n_0 d_0^2$ with quadratic polynomials of $h + n_0/d_0$ to experimental data. Recently, Nordquist *et al.*[10] reviewed the cavity depression depth data and concluded that Eq. [1] is not accurate for nozzle diameters less than 2 mm. They derived a new relationship based on a macroscopic energy balance.

HO YONG HWANG, formerly Graduate Student, Steel Research Centre, McMaster University, Hamilton, ON L8S 4L7, Canada, is now Research Engineer, ArcelorMittal Global R&D, East Chicago, IN 46312. GORDON A. IRONS, Dofasco Professor of Ferrous Metallurgy and Director, is with the Steel Research Centre, McMaster University. Contact e-mail: ironsga@mcmaster.ca

Manuscript submitted December 19, 2010.
Article published online December 1, 2011.

In contrast to the cavity depth, the jet cavity diameter is relatively insensitive to jet momentum at high values[7,11]; the cavity diameter is more dependent on the distance of the liquid surface from the nozzle and inclination angle. Banks and Chandrasekhara[6] also developed a relationship between cavity depth and diameter

$$\frac{d_c}{n_0} = A\sqrt{\frac{\dot{M}}{\rho_l g n_0^3}} \qquad [2]$$

where A depends on the assumed cavity shape; A is $\sqrt{16/\pi}$ for a paraboloid, $\sqrt{12/\pi}$ for an ellipsoid, and 2.9 for what they called a "deep cavity."

B. *Droplet Formation*

The ejection of the liquid phase by splashing is an important issue in the oxygen steelmaking process. This splashing generates the metal/slag/gas emulsion but also causes spitting of metal and slag from the vessel. Solidified slag droplets on the oxygen lance provide a protective layer to enhance lance life. Recently, slag splashing practices (with nitrogen after a heat is finished) have been developed to splash slag onto the vessel refractory walls to prolong their life. So splashing phenomena might have both beneficial and detrimental effects in steelmaking. Droplets can be generated by pressure fluctuations, horizontal and vertical cavity oscillations,[12] shearing by the gas stream, breakup of large droplets, entrainment into a gas stream,[13,14] and by the growth of the ripples.[15] Chatterjee and Bradshaw[16] determined the critical cavity depth to create droplets could be correlated with the Bond number and the Morton number for the liquid; the critical depths are 1.54 cm for water and 2.52 cm for iron melts.

To determine the critical velocity for droplet generation the nominal Weber number[17] and Blowing number[18] are useful.

$$\mathrm{We}_n = \frac{\rho_g u_s^2}{\sqrt{\rho_l g \sigma}} \qquad [3]$$

$$\text{Blowing number} = \frac{\eta^2 \rho_g u_s^2}{2\sqrt{\rho_l g \sigma}} = \frac{\eta^2}{2}\mathrm{We}_n \qquad [4]$$

The nominal Weber number is not a grouping of quantities usually reserved for Weber numbers ($\rho u^2/\sigma$), so the Blowing number terminology is preferred. Subagyo *et al.*[18] argued that the Blowing number is an estimate of how many times the critical velocity in the Kelvin-Helmholtz interface stability criterion has been exceeded. The analysis is based on the linear relationship between the vertical impinging gas velocity and the tangentially deflected velocity at the stagnation point.[19] The ratio of the critical tangential velocity to the axial jet velocity η is taken as 0.447, so that splashing by the Kelvin-Helmholtz instability occurs when the Blowing number is unity which is equivalent to a nominal Weber number of 10.[18,19] When viscous effects are included in the Kelvin-Helmholtz analysis for the air/water case, the critical velocity is decreased from 6.5 m/s[20] to 5.75 m/s.[21]

C. *Liquid Circulation*

In conventional BOF operations, the force from the oxygen jet is the only source of stirring; stirring is necessary to bring reactants such as carbon, silicon, and phosphorus into the reaction zones. From an industrial standpoint, it is well known that stirring from the top is poor, and this has prompted the development of a wide range of combined blowing practices. In these practices, varying amounts of gas are injected through the bottom, which stirs the steel much more effectively. Most studies of these phenomena have focused on measuring mixing times which is an indirect measure of the transfer of momentum from the gas to the liquid. Bath circulation was directly studied by Davenport by measuring the movement of plastic beads flowing with fluid by a video technique for a very limited set of flow conditions.[22]

The aim of the current work is to understand the response of the liquid surface in the gas jet impingement situation. Measurements of the cavity shape have been performed. The onset of splashing has been reexamined with the corresponding instability relationship and wave behavior. The extent of kinetic energy and momentum transfer from the gas to liquid has been measured. The current study benefited greatly from advances in digital photography and the use of digital particle image velocimetry (PIV) to measure the liquid velocity profiles in a plane of the vessel. Digital analysis techniques such as fast Fourier transforms (FFTs) and power spectral density analysis have permitted better characterization of the data than was possible in previous works.

II. APPARATUS AND EXPERIMENTS

A. *Apparatus*

A top gas jetting system was constructed that consisted of a cylindrical straight lance, flow meter, gas cylinder, and pressure regulator. The lance had inner and outer diameters of 2.85 and 4.76 mm, respectively. The lance length was made longer than the length for fully developed turbulent flow to ensure these conditions at the lance exit. The maximum velocity was approximately 300 m/s for which the Reynolds number is 57000. According to White,[23] the minimum pipe length to diameter ratio for fully developed turbulent flow is given by $L/d = 4.4\mathrm{Re}^{1/6}$. Therefore, the minimum required length is approximately 8 cm, but a 50 cm length was used so that the lance height could be changed conveniently.

A DataMetrics 810LM-PAX hotwire type flow meter (DataMetrics Corp., Orlando, FL) was used to measure the gas flow rate; the minimum and maximum capacities were 10 and 500 standard liters per minute (SLPM), respectively. The flow meter was calibrated with a Precision Scientific (Chicago, IL) wet test meters. The gas jet behavior depends, to some extent, on the nozzle tip geometry, so the centerline jet velocity was measured with a pitot tube. The measured data were compared with those of Wygnanski and Fiedler,[24] and the data were fitted to linear regressions for the free jet and wall jet configurations. The following relationships were

obtained from the calibration procedure. For the wall jet, the distance from the wall was half the diameter of nozzle, 2.4 mm.

$$\text{free jet:} \quad \frac{u_0}{u_m} = 0.185\frac{x}{d_0} - 1.141 \qquad [5]$$

$$\text{wall jet:} \quad \frac{u_0}{u_m} = 0.180\frac{x}{d_0} - 1.727 \qquad [6]$$

The gas cylinder pressure was maintained at 345 kPa throughout the experiments. Preliminary tests were performed with a cylindrical tank of 45 cm diameter and 50 cm height filled with tap water to 20 cm. However, the jet cavity geometries were disrupted by the waves from the vigorous splashing. Because the jet cavity shapes depended mainly on the impinging jet pressure, the liquid tank dimension did not have much effect when the tank size was much greater than the cavity. Therefore, in the reported experiments, a tank of 50 × 50 × 50 cm filled with distilled water to 20 cm height was used with a wall jet configuration to extract better geometrical information. Details of the tank and gas systems are illustrated in Figure 1.

The jet cavity image was recorded with a Sony DCR-TRV 80 HandyCam (Sony, Tokyo, Japan); the frame rate was 30 frames/s. To enhance the contrast at the free surface line, the camera aperture was maintained with low values and a 200 W lamp was used on the back lower side of the tank to illuminate the surface. The digital images were stored as JPEG image files for later analysis.

The water flow field was measured with PIV using the LaVision integrated system (LaVision GmBH, Goettingen, Germany). The system consist of a Nd-YAG green (532 nm) pulsing laser unit, 1.4 megapixel digital camera, and PIV control and analysis software. The pulsing laser has 100 mJ maximum power and minimum time interval was 0.5 μs. The double-pulsed laser was synchronized with the digital camera shutter with a special time control—frame straddling, which is well described by Gharib and Daribi.[25] The camera had progressive scan interline transfer charge-coupled device type and it was double shuttered for the frame straddling mode. Dantec (Dantec Dynamics A/S, Skovlunde, Denmark) hollow glass beads of 9 to 13 μm were used as the seeding particles. As shown in Figure 2, the laser beam was converted to a sheet of light using a cylindrical lens and adjusted to cover the whole area of interest. The 45-cm diameter cylindrical tank, filled with distilled water to 20 cm, was contained inside of larger square tank to minimize the distortion of the image and excessive expansion of laser light sheet. The laser light sheet was aligned vertically and the particle images were taken at the right angle from this illuminated plane.

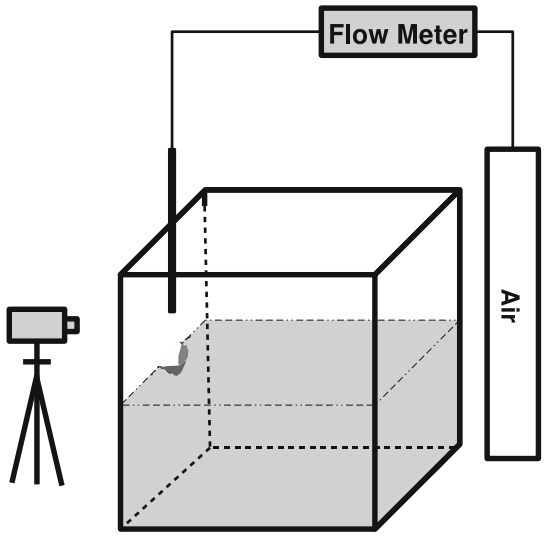

Fig. 1—A wall jet cubic tank experimental setup that is used in the experiments for the video measurement of surface geometry.

B. *Surface Geometry Measurement*

For the surface geometry measurement, the flow rate was controlled between 10 and 100 SLPM, and the lance distance from the liquid surface varied from 6 cm to 24 cm. The video images taken by the camera were stored and image filtering was applied to emphasize the free surface interface. From the filtered images, the free surface line was digitized. A series of 60 sequential images over 2 seconds were digitized for each experimental condition, and each digitized surface profile was analyzed to extract the geometrical data. Figure 3 shows a schematic diagram of digitization and definition of surface geometrical variables. The digitized data were interpolated with a cubic spline using a finer interval than the experimental data interval and were used for a subsequent analysis. The time series of depth of cavity,

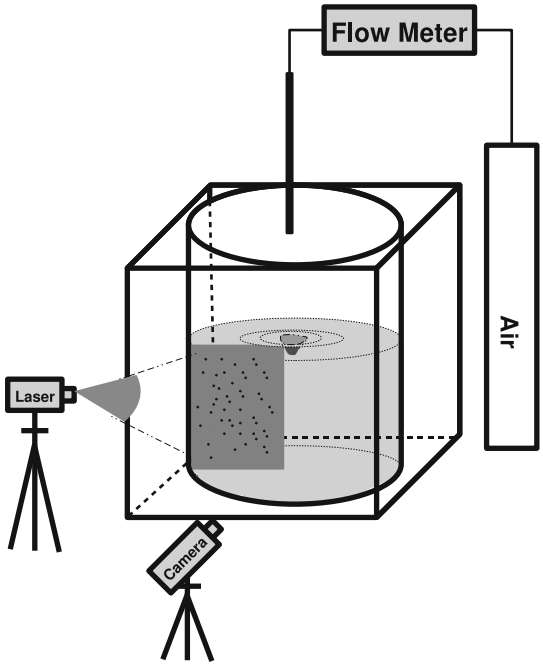

Fig. 2—A PIV setup. The laser sheet was aligned vertically and the illuminated particles were photographed with the digital camera, which was at right angle to the light sheet.

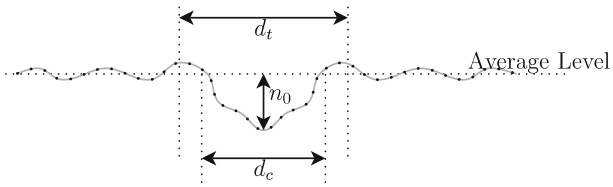

Fig. 3—Schematic diagram of analysis of digitized surface profile data.

width of cavity at the average surface level, width of cavity at the top elevation position, and horizontal position of deepest cavity position were stored and analyzed with FFT and power spectral density (PSD) functions, as will be discussed subsequently.

C. *PIV Measurement*

In the PIV technique, a cross-correlation analysis is used to determine how far the particles in the image have moved.[25,26] The selection of interrogation window size must consider the flow velocity range; a recommended criteria according to Kean and Adriantems[27] is 0.1 pixel $< \Delta x < 0.25 d_{\text{int}}$, where d_{int} is the interrogation window size. For each experimental condition, the PIV measurements were made 3 to 5 minutes after starting blowing to establish steady-state liquid circulation velocity. Preliminary test measurements were performed for each PIV measurement with an approximate time step. From the measured minimum and maximum velocities in the test, the proper time step was determined and the measurement was repeated with it. To obtain the best picture, the camera aperture and laser power were adjusted for each flow rate and lance height; the time step ranged from 3 to 30 ms. The images were analyzed with DaVis software of LaVision. A 64 × 64 pixel interrogation window was selected and a single-pass algorithm was used. A median filter was applied to each velocity analysis, and statistically spurious vectors are eliminated and replaced by interpolations. The 20 vector measurements were averaged and the cavity surface and gas side were masked.

III. RESULTS AND DISCUSSION

A. *Surface Geometry and Dimensionless Relationships*

Figure 4 shows that the mean depth increases with gas flow rate and that the fluctuations in depth increase with it as well. Figure 5 shows that the mean diameter d_c (at the initial surface level) and top lip diameter d_t follow each other closely over the range of flow rates and lance heights. Contrary to the findings of Cheslak *et al.*,[11] the slope of width change was affected by the flow rate. The decrease of the slope in the higher flow rate is considered to be associated with the regime change[4] to the splashing mode as reviewed in Section I.

Banks and Chandrasekhara's[5] similarity relationship, in Eq. [1], was modified slightly to represent the linear functional behavior between the length group and the momentum group. The square root of the slope is the turbulent gas jet constant K

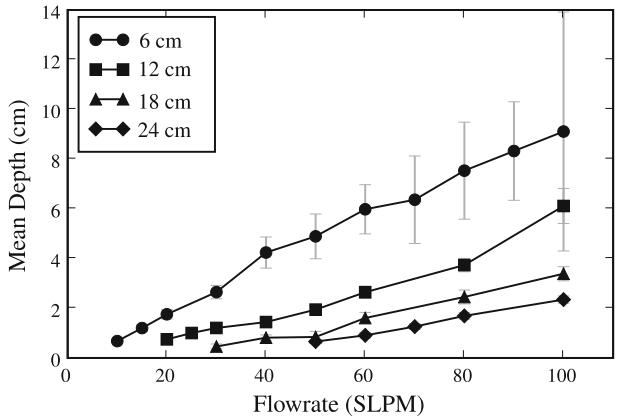

Fig. 4—The mean jet cavity depth *vs* gas flow rate, the error bar is ±1 standard deviation for lance heights 6, 12, 18, and 24 cm.

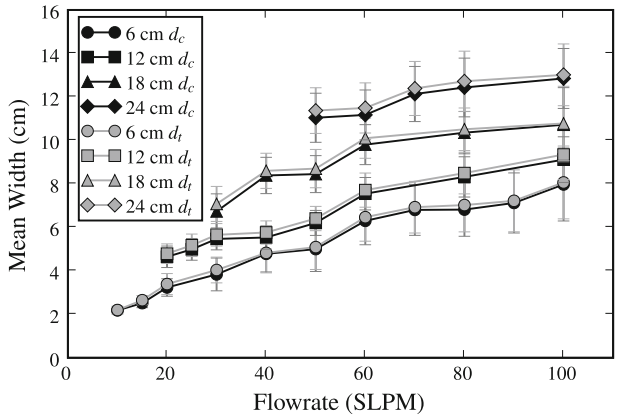

Fig. 5—The mean jet cavity width and lip width *vs* gas flow rate; the error bar is ±1 standard deviation for lance heights 6, 12, 18, and 24 cm.

$$\frac{n_0}{h}\left(1+\frac{n_0}{h}\right)^2 = K^2 \frac{\dot{M}}{\pi \rho_l g h^3} \qquad [7]$$

The linear regression (Figure 6) shows that the slope K^2 is 60.9 and corresponding K value is 7.81 ± 0.05. This value is slightly higher than other reported values (5.5 to 7.5).

The impact point velocity, *i.e.*, the vertical velocity that the jet would have at the height of the liquid if it were not present, was obtained from the calibration procedure with the pitot tube. As described by Banks and Chandrasekhara,[5] the local force balance at the stagnation point is the starting point of their theoretical derivation for their analysis. The local force balance between the vertical kinetic energy and the potential energy leads to the local modified Froude number

$$\text{Fr}_{lm} = \frac{\rho_g u_g^2}{\rho_l g n_0} = 2.0 \qquad [8]$$

Figure 7 shows the variation of the local modified Froude number with the computed impact velocity and the measured depth of penetration. There is some scatter of the data because the depth of penetration fluctuates

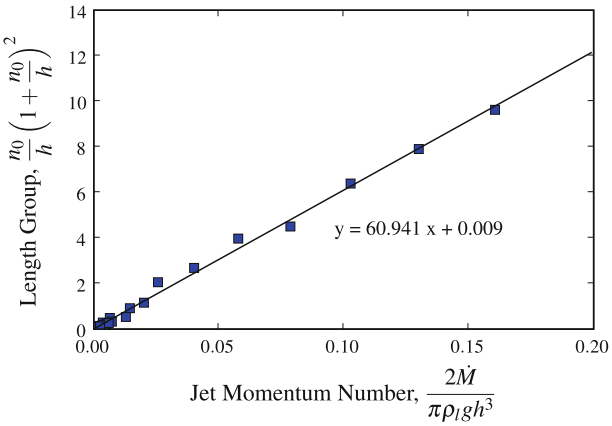

Fig. 6—The deep cavity relationship from Eq. [1] was modified and used to observe similarity behavior. The horizontal axis is the momentum group and vertical axis is the length group. The slope is the square of the turbulent gas jet constant.

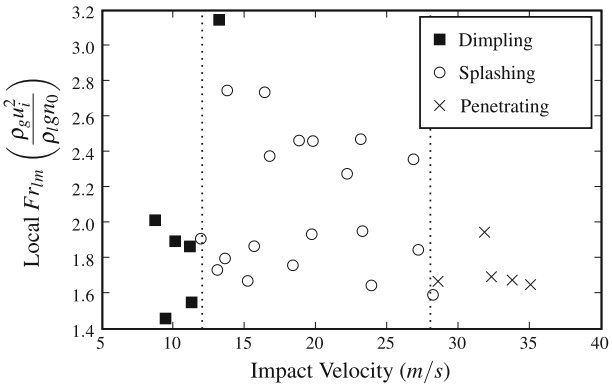

Fig. 7—Local modified Froude number as a function of impact velocity. The data are clustered around modified Froude numbers of 2 for dimpling and penetrating range.

considerably, but the scatter diminishes as the impact velocity increases and the values converge to a value somewhat below 2. Beyond the Splashing stage, the decrease in variation is clear, which means the vertical force balance becomes more dominant. There is some discrepancy between Molloy's[4] criteria for the transitions between the stages: dimpling to splashing (13 compared with his 15 m/s) and splashing to penetrating (28 compared with his 75 m/s). The discrepancy comes from the difference in the calculation of the impact point velocity. Molloy used the initial nozzle to undisturbed liquid surface distance, but this study used the actual distance from the nozzle to the depressed liquid surface point.

Qian *et al.*[9] defined a new parameter F_q to provide a better correlation between the dimensionless momentum and distance groups. At higher flow rate and deeper penetration, F_q increases quadratically with dimensionless distance, which was defined as $(h + n_0)/d_0$. The fitted equation was

$$F_q = 0.024\left(\frac{h+n_0}{d_0}\right)^2 + 0.0072\left(\frac{h+n_0}{d_0}\right) + 0.84 \quad [9]$$

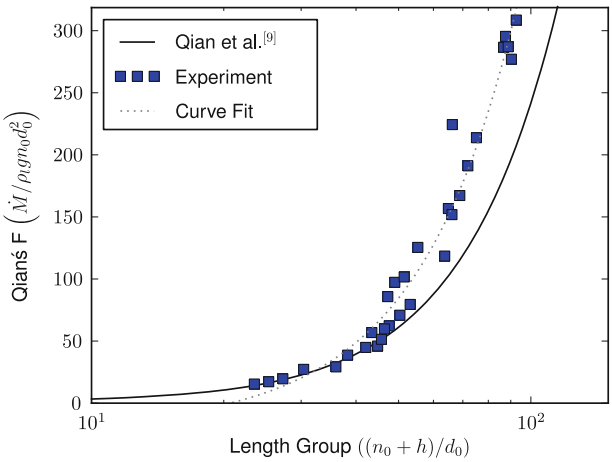

Fig. 8—A comparison with Qian *et al.*'s correlation F_q showing its deviation from the data for length groups over 40.

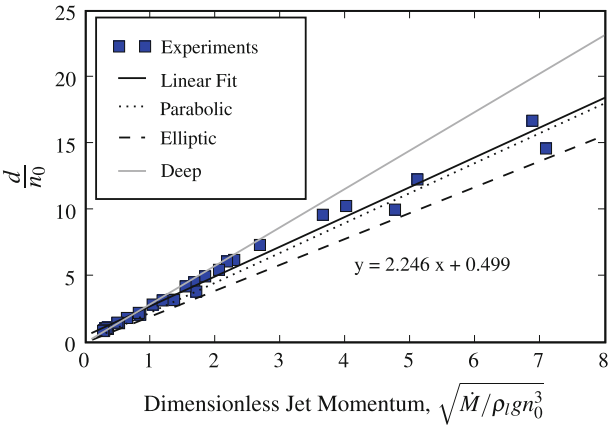

Fig. 9—A plot of dimensionless momentum and cavity aspect ratio. The current experiments show the overall cavity shape closer to parabolic.

Figure 8 shows Eq. [9] and the experimental results of this study. Qian *et al.*[9] based their correlation on measurements up to dimensionless distances of 50. The current experiments and Eq. [9] match up to $(h + n_0)/d_0 = 40$. However, for higher flow rates, the experimental results deviate from Eq. [9]. Therefore, a new regression formula was obtained from the current data.

$$F_q = 0.0358\left(\frac{h+n_0}{d_0}\right)^2 + 0.353\left(\frac{h+n_0}{d_0}\right) - 22.615, \quad \text{rms} = 3.17 \quad [10]$$

Banks and Chandrasekhara[5] derived a dimensionless relationship of the ratio between the cavity width and depth assuming three different cavity shapes, elliptic, parabolic, and deep shape. Figure 9 shows the plot of the width-to-depth ratio against the dimensionless momentum. The slope depends on the assumed cavity shape. The current cavity width-to-depth ratio is closer to the parabolic shape. Contrary to Turkdogan[7] and Cheslak *et al.*,[11] the cavity width depended on the jet

momentum. In the penetrating regime, some data have a narrower cavity width because the lip was directed inward, but the average width increased with flow rate.

B. *Kelvin-Helmholtz Instability*

As discussed in Section I, a Blowing number of unity corresponds to the onset of the Kelvin-Helmholtz instability to produce droplets. The ratio of the tangential velocity to the axial velocity η has been taken as 0.447 based on previous work for gas jets impinging on solid flat plates[18]; it has not been determined for fluid surfaces. Multiplying this value by the vertical velocity for splashing in the current work, 13 m/s, produces 5.81 m/s for the critical tangential velocity. This value is much closer to the critical velocity from the Kelvin-Helmholtz theory accounting for the viscosity of water, 5.75 m/s,[21] than the value for inviscid ones, 6.50 m/s.[20] Therefore, even with some discrepancy in the deflection velocity, the Blowing number can be used for the criteria of how many times the critical Kelvin-Helmholtz instability has been exceeded, as proposed originally.[18]

The onset of splashing is difficult to determine because there is a distribution of droplet sizes. Small droplets were generated around the waves even at a low flow rate; this was found when a paper tissue became wet when held near the interface, even though droplets could not be seen by eye. Therefore, the onset of splashing was determined when the surface starts to eject some visible drops (3 to 5 mm) around the perimeter of the cavity. The flow rate for the onset of splashing was summarized in Table I. Figure 10 shows that splashing begins when the Blowing number is approximately 0.7 to 0.8.

At higher flow rates, the jet penetrated into the liquid surface and bubbles were entrained into the water. This penetration was observed only in the 6-cm lance height case above the 60 SLPM flow rate. In He and Standish's[17] analysis, a sharp increase of droplet generation rate occurred around the nominal Weber number of 40, which corresponds to Molloy's penetrating regime. The Blowing number is approximately 4 when the impact velocity is 28 m/s (penetrating criterion). Molloy[4] indicated that the splashing is reduced in the penetrating regime. That finding may be explained with the current observations in that the generated splash may not be able to escape a deep cavity, but larger wave generation by penetration and corresponding bubble entrainment around the jet cavity may contribute to the generation of splash by this different mechanism.

Table I. The Flow Rate at the Onset of Splash for Each Lace Height

Lance Height (cm)	Onset Flow Rate (SLPM)
6	15
12	30
18	45
24	60

The critical depression depth (cavity depth at the onset of splashing) is another important parameter. The previously reported critical depression depth was 1.54 cm for the water–air system.[16] However, this value depends on the jetting condition such as jet momentum and lance height, as shown by Figure 11. The critical depth decreases slightly when the lance height increases. Chatterjee and Bradshaw[16] observed this slight decrease of critical depth, but they interpreted this depth simply as an "inherent property of the liquid." Larger cavity width gives an impinging jet more distance over which to transfer momentum to the liquid for the growth of unstable waves. According to the analysis of Kitscha and Kocamustafaogullari[28] and Funda and Joseph,[21] the stable and unstable wave conditions can be determined from a force balance, but in the actual critical wave, phenomena require time and distance to grow. So in their analysis, the maximum growth rate does not occur at the critical wavelength but at smaller wavelengths that have larger growth rates. Therefore, this interpretation may explain the decrease of critical depression depth with an increase in the cavity

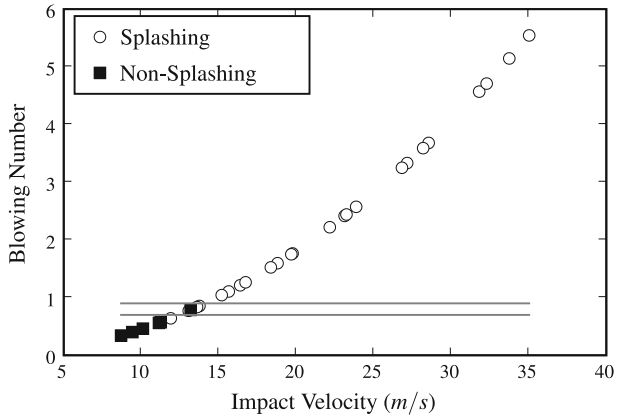

Fig. 10—The change in the Blowing number with the impact velocity. Splashing begins at approximately 0.7 to 0.8.

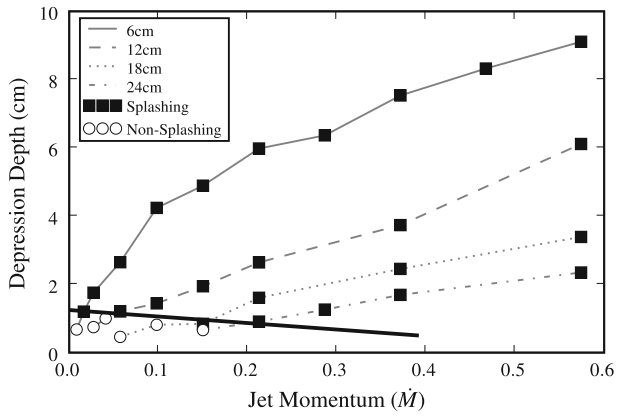

Fig. 11—Depression depth as a function of the jet momentum. The solid line shows that the critical depression depth for splashing decreases as the lance height increases.

width; there is more distance and time for the jet to disturb the surface.

C. *Spectral Analyses of the Interfaces*

An FFT was applied to the time series of measured variables and the surface profiles to determine whether characteristic frequencies and wavelengths exist. For the lowest lance 6 cm, the Fourier transform of cavity depth (Figure 12) shows a wide range of frequencies. For the horizontal position of cavity depth, 2 Hz was pronounced in 6-cm height case, but a characteristic frequency was not dominant in the other lance heights (12, 18, and 24 cm). As the lance height was increased, lower frequencies of 4 to 8 Hz became more dominant for cavity depth and width; this is generally consistent but somewhat lower than in the previous work, 5 to 12 Hz.[13]

D. *Wavelength Variations*

The Blowing number analysis shows that this system has a strong relationship with the Kelvin-Helmholtz instability. According to this theory, the gas momentum will cause waves on the surface that are stable at a low gas velocity, but as the velocity is increased, they move into unstable smaller waves that disintegrate into the stable range. At some critical velocity, the waves grow so rapidly they cannot return to the stable range. This wave behavior can be observed qualitatively in Figure 13. The wavelength is relatively large in Figure 13(a), and as the gas flow rate increases, the wavelengths become smaller as in Figure 13(b).

As the gas velocity increases, the situation changes in the penetrating regime. The gas penetration into the cavity surface leaves a deeper dimple inside the jet cavity that is fluctuating, and this dimple requires some time to recover to the average shape of the cavity surface. Sometimes, this deeper part of the cavity is trapped as a bubble by the returning flow. Consequently, the cavity surface contains these deeper penetrations with longer wavelength fluctuations, and they are grouped with smaller waves that were generated from the returning trapped bubbles to the surface. This is observed in Figure 14 for the 6-cm height case.

These observations provide a qualitative perspective, but this cannot explain the connection with Kelvin-Helmholtz instability. The simple application of the FFT to the digitized cavity shapes did not show distinguishable results for the typical wave numbers because of the overwhelming contribution of large waves to its power. Therefore, a PSD function was used for the analysis. For the definition and the physical meaning of PSD, see the Appendix.

As indicated by Elson and Bennet[29] in their surface profile analysis, a PSD of a single profile does not give a good estimation; ensemble averages must be used. For this purpose, 60 digitized surface profiles were used to find the average. Figure 15 shows the ensemble-averaged PSD surface variation with wave number ($k = 2\pi/\lambda$). At a high lance height, the PSD plot shows only small fluctuations for the highest flow rates, so only the

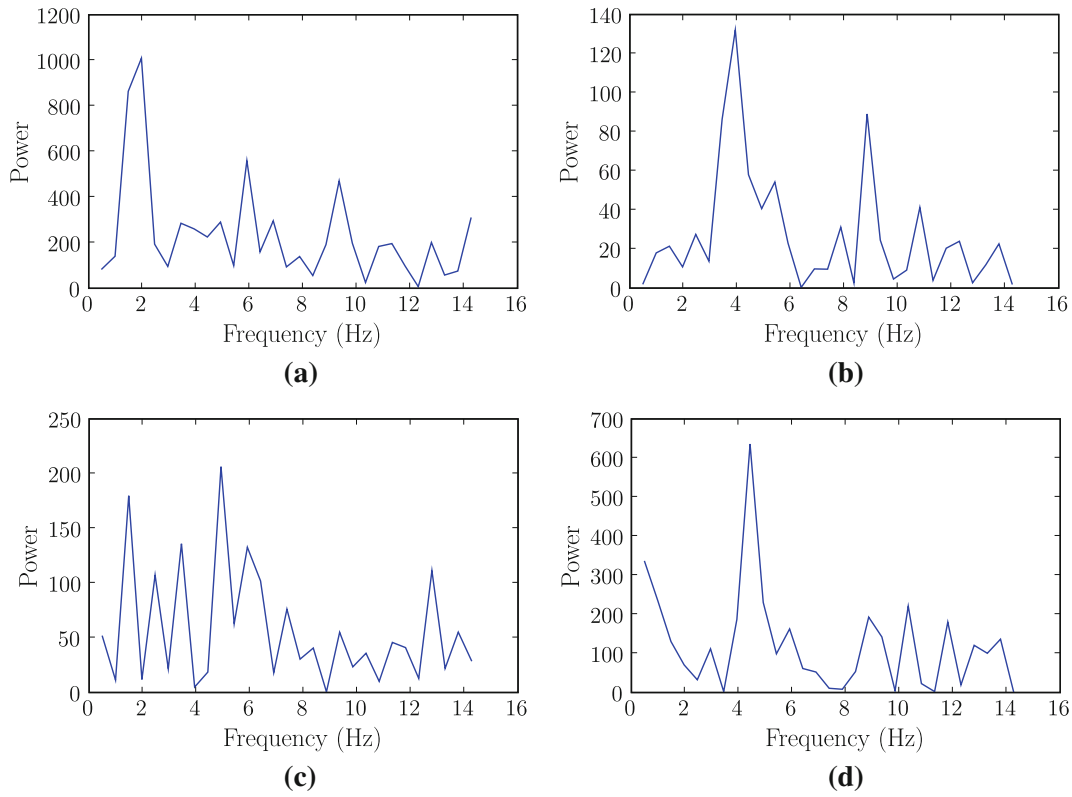

Fig. 12—Fast Fourier transform of time series of cavity depth change for 80 SLPM cases. (*a*) 6 cm, (*b*) 12 cm, (*c*) 18 cm, and (*d*) 24 cm.

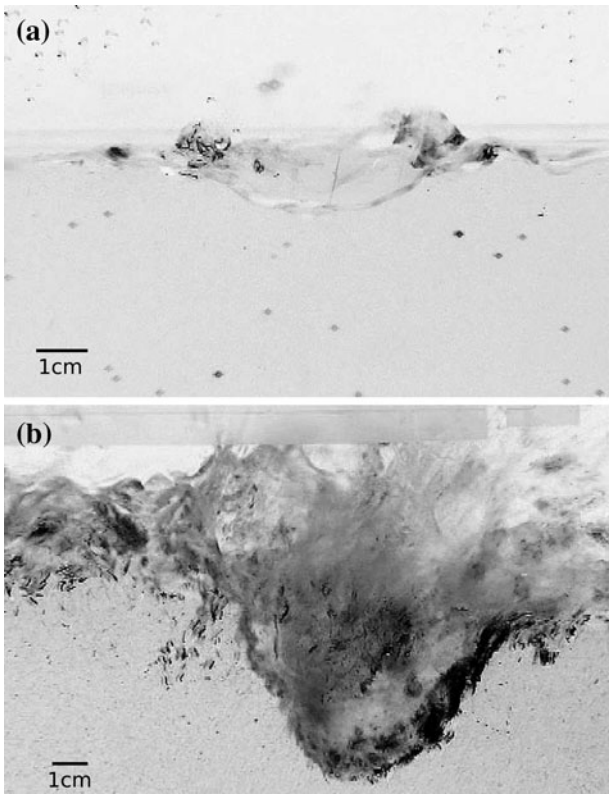

Fig. 13—An example of wavelength disintegration. As the flow rate increases, the typical wavelengths of the ripples in the cavity decrease. The pictures are from the 12-cm lance height. (*a*) Low flow rate, 30 SLPM and (*b*) high flow rate, 100 SLPM.

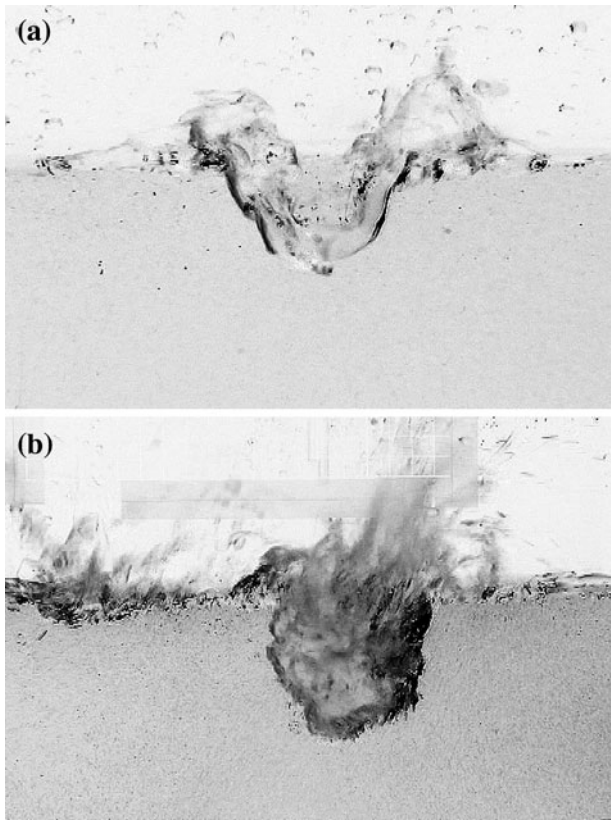

Fig. 14—A comparison between the splashing regime (*a*) and the penetration wave behavior (*b*). In the penetration range, the surface the cavity contains small ripples. The pictures are from the 6-cm lance height case. (*a*) Splashing, 30 SLPM and (*b*) penetration, 80 SLPM.

6-cm case is shown in Figure 15. At low flow rates, there are no distinguishing features in the distributions; straight lines are observed in the plot. Close to the penetrating regime (up to 50 SLPM), there is more power in the waves with wave numbers of approximately 80 cm^{-1} or wavelength of 0.785 mm, and the major parts of wave number keep increases until the flow reaches to the penetration range.

Further into the penetrating regime, the power distribution shifts to lower wave numbers of the order of 30 cm^{-1} or wavelengths of 0.1 cm (*i.e.,* the peaks in the curve shift to lower wave numbers as the flow rate is increased). This range of wave number is comparable with the maximum growth factor range computed from the viscous potential theory,[21] which is caused by the penetration that produces larger wavelengths. In this regime, the wave behavior is affected more by the penetration, trapped voids, and returning bubbles than the shearing action of the gas. That is to say, the surface wave motion becomes less influenced by the Kelvin-Helmholtz instability, which arises from the differential velocity of stratified fluids. When upward returning gas flow cuts liquid ligaments extending inward to the cavity, the bulk fluid was accelerated upward and disintegrated into droplets, as described by Peaslee and Robertson.[13] This case is analogous to liquid drops in a fast gas stream as is considered by Joseph *et al.*[30] Therefore, Rayleigh-Taylor instability is more appropriate than Kelvin-Helmholtz instability.

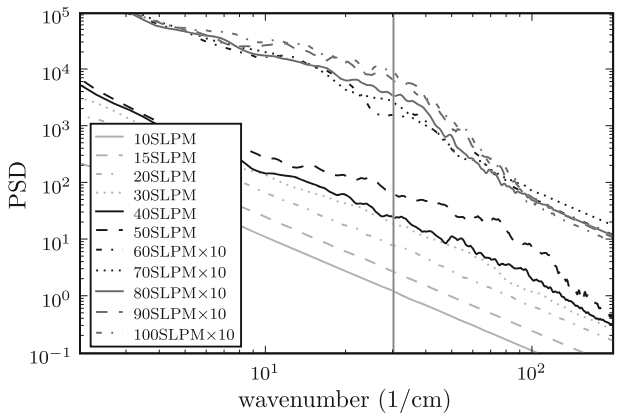

Fig. 15—Power spectral density dependence on the wave number for 6-cm lance height. The wave number increased until the Penetration regime, and the wave number shifts to a lower range after the Penetration regime (above 60 SLPM). Note that the lines from 60 SLPM to 100 SLPM are shifted upward by 10 for clarity.

E. *Temporal Oscillation of the Surface*

It is important to control oscillations in a metallurgical vessel for stability in operation. Typical temporal oscillation frequencies have been reported in many papers.[13,31,32] The measurements from this study match the range in other studies, 4 to 12 Hz. However, a

dominant frequency and a systematic relationship with lance height could not be found. Uncertainty in the relationship between the frequency and the lance height appears in the literature as well; Lee *et al.*[31] reported a strong linear relationship between those two variables, but Lee *et al.*[32] indicated that the wave motion is "indifferent to nozzle height and angle."

To determine a characteristic frequency of each impinging condition, a PSD analysis was applied to the times series of the measured surface geometrical variables. Figure 16 shows the PSD of each time series of the vertical cavity depth, cavity width, and the horizontal position of cavity tip. Characteristic frequencies could not be found with this method. However, the spectral decay behavior (the slope of the graphs) all has the same value, close to –5/3. Surface elevation spectra have been measured by several researchers, and they all show different slopes in PSD. Metcalf *et al.*[33] measured a surface elevation and pressure spectra around an underwater foil in turbulent flow; their slopes were –2 and –5/3 for surface elevation and pressure, respectively. Zarruk[34] measured surface elevation with PIV images with waves from a wave generator underneath of the surface; the slope taken from their figures was approximately –3. Mitsuyasu and Honda[35] measured the water surface elevation spectra of waves generated from wind shear; the slope was –2 to –3, but the slope was reduced in the presence of surfactants. Lommer and Levinson[36] reported –17/6 in their vertically shaken vessel. Weak turbulence theory[37,38] indicates the slope should be –17/6 for capillary waves and –4 for gravity waves. Dabiri[39] indicated that the surface elevation is related directly to pressure for low Froude number flow. They interpreted the surface elevation spectra as pressure spectra and obtained a slope –10/3, which they compared with an isotropic pressure spectra theoretical slope of –11/3.[40] So in all of these studies, the slope ranged between –2 and –4, depending on the flow conditions.

In this impinging jet situation, the cavity surface depth was interpreted with force balance at the stagnation point, so it is reasonable to assume that the fluctuations in the shape are caused by turbulent fluctuations in gas velocity and pressure. Near a surface, the isotropic turbulence behavior breaks down and anisotropy in length scales have been reported by Handler *et al.*[41] Some direct numerical simulation results show anisotropic turbulent behavior around a surface.[42] Brumley and Jirka[43] observed an attenuation of vertical velocity spectra close to the free surface. Guo and Wood[44] measured time spectra of velocity and pressure in a gas jet impinging on a flat solid plate and observed attenuation of the vertical velocity and pressure spectra close to the plate. Therefore, the –5/3

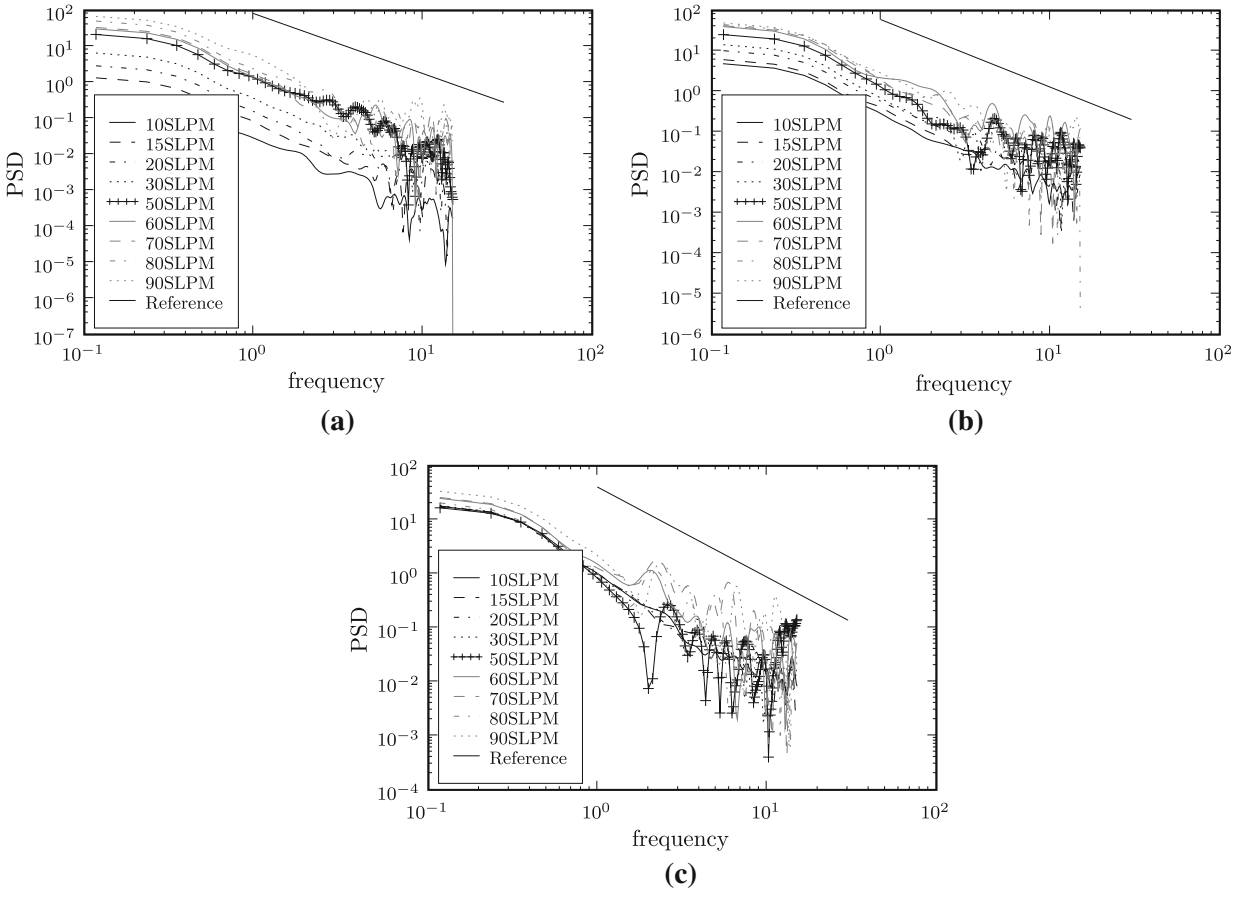

Fig. 16—Power spectral density of cavity geometrical variables for a lance height of 6 cm, the slope of the reference line is –5/3. (*a*) Vertical depth, (*b*) width, and (*c*) horizontal position of cavity tip.

slope of time spectra in this study is thought to be the result of the attenuation of the turbulent velocity and pressure spectra close to the surface.

F. *Wall Jet Experimental Issues*

As indicated in Section II, the surface geometry measurements were done in the wall-jet setup (Figure 1). Preliminary full three-dimensional (3D) cylindrical measurements were used to determine the depression depth only, but the detailed wave behavior inside cavities could not be obtained; it was difficult to determine which wave comes from which part of paraboloid section viewed from outside of the vessel.

The wall jet behaves differently[45–47]; there is larger span-wise expansion and the vertical velocity profile along the wall. Wall jet measurements from the literature[46,47] and the calibration in this work show –1.066 to –1.16 exponent to the lance height for the centerline velocity decay; for the circular 3D jet case, it is –1. So the dimensionless relationship for depression depth (Figure 6) shows almost identical behavior with previously reported result for the full 3D case.[48] The jet expansion is wider in for the wall jet, so a wider cavity shape would be expected. However, the results of Figure 9 show good agreement with the parabolic shape reported by Banks and Chandrasekhara. The agreement may be fortuitous because there is some discrepancy regarding the cavity width between investigators; some claim it is independent to the flow rate.[7,11] The current experiment was neither fully 3D nor two dimensional, so the open side away from the wall may have allowed the cavity to behave like a fully 3D case, but this requires subsequent investigation.

G. *Liquid Velocities*

Figure 17 shows examples of PIV measurements for low and high flow rates. These measurements were made when the flow conditions were established at a steady state. As expected, the liquid moves away from the cavity depression at the center of the tank and moves toward the vessel walls. A recirculation area was established near the walls.

H. *Kinetic Energy Transfer Efficiency*

To assess the extent of kinetic energy transfer from the gas to the liquid, an energy transfer index **I** was defined, assuming cylindrical symmetry of velocity and neglecting angular velocity

$$\mathbf{I} = \frac{\int \rho_l u^2 dV}{\dot{E}_{in}} \qquad [11]$$

It is the ratio between the kinetic energy in the sum of the fluid and the input kinetic energy flux input rate at the undisturbed initial liquid level, which is obtained as follows:

$$\dot{E}_{in} = 0.136 \rho_g K^3 \frac{Q^3}{\pi d_0^3 h} \qquad [12]$$

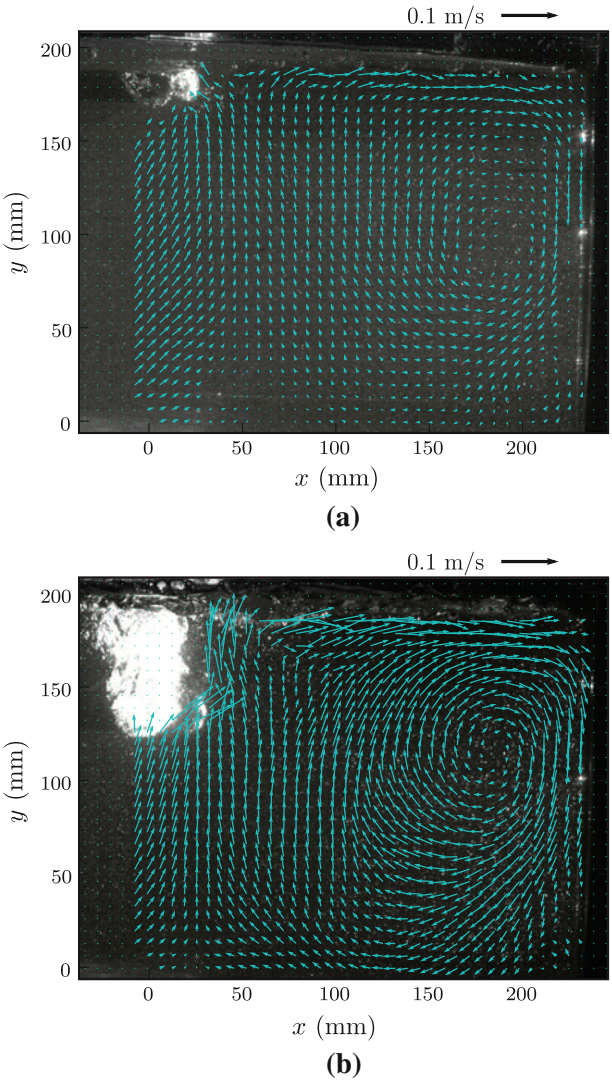

Fig. 17—Examples of PIV measurement velocity vectors. The background image is one of the PIV pictures from the measurement. (*a*) 6 cm, 40 SLPM and (*b*) 6 cm, 90 SLPM.

where K is the turbulent jet parameter (7.81) and Q is the gas flow rate. It is difficult to define the energy input from the gas to liquid because the jet kinetic energy of the initial jet is degraded by the entrainment of stagnant surrounding air and by the production of turbulence,[5] so an appropriate kinetic energy flux at the point of impingement must be determined. The axial gas velocity profile has Gaussian shape, and it is a simple matter to demonstrate that the summation of the kinetic energy from the jet centerline to the half of the maximum velocity profile includes more than 95 pct of the total kinetic energy. Therefore, the kinetic energy input rate at the impingement point $\dot{E}_{\text{in}}$ is given by

$$\dot{E}_{\text{in}} = \int_0^{2\pi} \int_0^{r_{1/2}} \frac{1}{2} \rho_g u^2 u r dr d\theta \qquad [13]$$

$$u = u_m e^{-0.693\left(r/r_{1/2}\right)^2} \quad [14]$$

Nakanishi *et al.*[49] defined the specific energy dissipation rate for top-blown vessels.

$$\varepsilon = 0.4530 Q_T d_0 u_0^2 \cos^2\theta / W / h \quad [15]$$

where W is liquid weight. This concept is similar to the energy transfer index. $\dot{E}_{in}$ can be rearranged into a different form

$$\dot{E}_{\text{in}} = 8.5 \times 10^{-3} K^3 \rho_g Q d_0 u_0^2 / h \quad [16]$$

If the jet is vertical, then the cosine term drops out. Assuming that the flow is incompressible, the mass flow rate $\rho_g Q$ can be replaced with normal Q_T. The numerical coefficients depend on the nozzle conditions. The specific energy dissipation rate is referenced to the bath weight W so for fixed nozzle conditions, kinetic energy input $\dot{E}_{in}$ is proportional to W, and the current energy transfer index **I** can be written as follows:

$$\mathbf{I} = \frac{\int \rho_l u^2 dV}{\varepsilon W} \quad [17]$$

Figure 18 shows the energy transfer index over the whole liquid domain calculated from the PIV data. The energy transfer is more efficient at a higher lance height within the present experiments, but the flow rate did not have much effect on it. Davenport *et al.*[22] reported that the bath circulation was greater at higher lance heights for equivalent kinetic energy levels at the impinging point. The current analysis supports their claim. These findings may be explained as follows. When the lance height is low, there is deeper penetration, so the gas velocity is higher and the contact area between the gas and liquid is small. More splashing and bubble formation occurs, which consumes extra energy. At higher lance heights, with the same initial jet exit velocity, the cavity will be wider, providing larger contact area for increased momentum transfer. For extremely high lance heights, it is expected that eventually a decrease will occur in the energy transfer index because of the consumption of the kinetic energy by the production of turbulence. This finding is consistent with the fact that the slag splash practice has optimum lance height when the gas flow rate is fixed.[50]

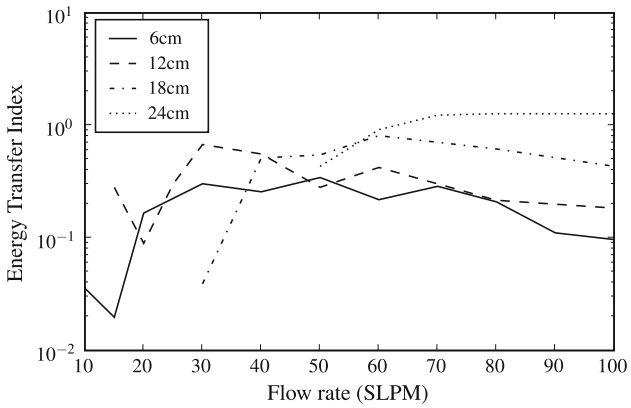

Fig. 18—A comparison of the sum of energy transfer parameter I.

I. *Momentum Transfer around the Jet Cavity*

Kinetic energy balances, such as the specific energy dissipation or the energy transfer index, discussed in the previous section have limited value as a tool for process analysis for two reasons. First, kinetic energy is always degraded by several phenomena, and second, force or momentum balances are the basis of dynamic similarity. Therefore, the momentum balances presented in this section are potentially much more useful for scaling the results to industrial levels. As mentioned in Section I, the transfer of momentum from the gas to the liquid is important for mixing in BOFs. The transfer was assessed in two ways, first by measuring the velocity in the immediate vicinity of the cavity u. As a result of fluctuations in the cavity shape and position, and limitations of the PIV technique the liquid surface velocity could not be measured. Therefore, an area for investigation close to the interface was selected, and the velocity values averaged in this region (Figure 19(a)). The second measurement was the volume-weighted

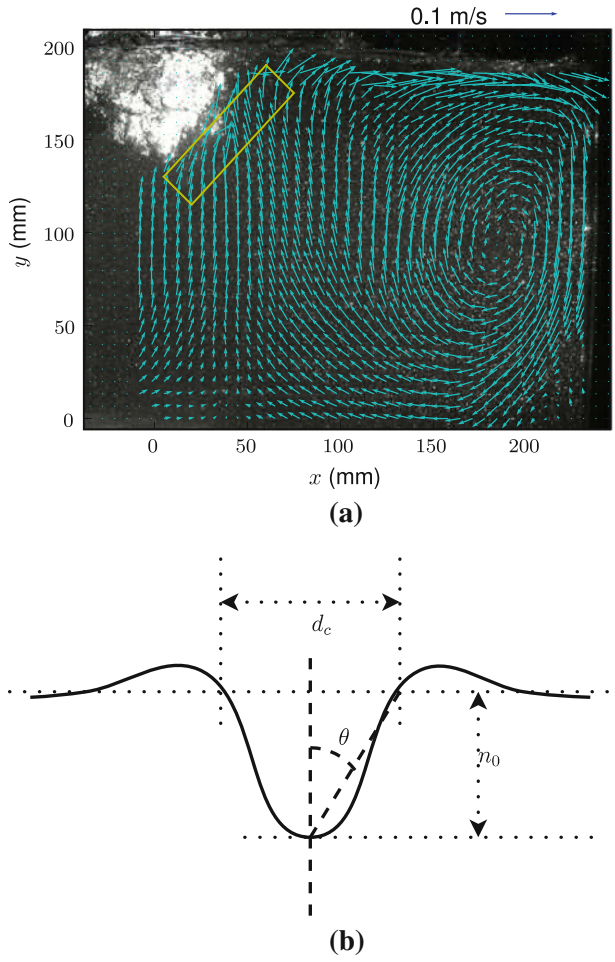

Fig. 19—The area of local velocity investigation and an illustration of the approximation of cavity angle. (*a*) Local velocity and (*b*) angle.

average of the liquid velocity $\overline{u}$ in the entire liquid domain.

These velocities will be related to the blowing conditions. Assuming that the momentum transfer inside of the cavity is dominated by a shear stress balance, the momentum balance is

$$\mu_1 \frac{u_1 - u_s}{\delta_1} = \mu_2 \frac{u_s - u_2}{\delta_2} \quad [18]$$

where δ_1 and δ_2 are boundary layer thicknesses for each phase, and u_1 and u_2 are tangential velocities around the cavity. This yields a simple linear relationship between the two tangential velocities

$$u_2 = Au_1 + B \quad [19]$$

As in the Blowing number analysis, it will be assumed that a linear relationship exists between the deflected or tangential gas velocity and the impinging gas velocity ($u_1 = \eta u_s$). It was shown in Figure 7 that a local modified Froude number similarity relates the impinging gas velocity with the depression depth ($\rho_g u_s^2 / \rho_l g n_0 = 2$); thus, u_1 is proportional to $\sqrt{n_0}$ and these substitutions can be made in Eq. [18]

$$u_2 = A' \sqrt{n_o} + B \quad [20]$$

According to Eq. [20], a linear relationship is expected between the liquid velocity and the square root of the depression depth.

Figure 20(a) shows the relationship between the measured velocity near the cavity u and the square root of depression depth. In general, there is a linear trend within the experimental scatter in the data. The other observed trend is that for an equivalent penetration depth, more momentum transfer is observed for a higher lance position, which seems counterintuitive. This finding can be explained by the same argument made in the previous section: There is more momentum transfer for wider cavities. Figure 20(b) for the average liquid velocity shows similar trends with the square root of the cavity depth.

These findings imply that some cavity shape factor can influence the momentum transfer to the liquid. Several functional relationships were investigated, and the nomenclature is illustrated in Figure 19(b). The angle of cavity slope was obtained from $\tan^{-1}(d_c/2n_0)$. The contact distance increases as the angle increases and as cosine θ decreases. Figures 21(a) and (b) show that

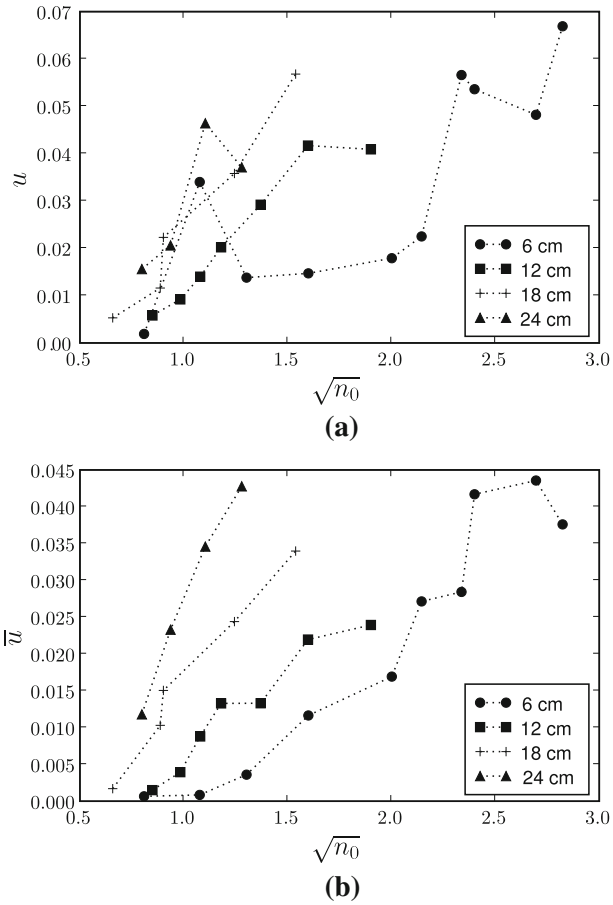

Fig. 20—The measured local characteristic velocity and depression depth, and each lance height shows linear relationship between the velocity and square root of depth. (*a*) Local velocity, (*b*) average velocity.

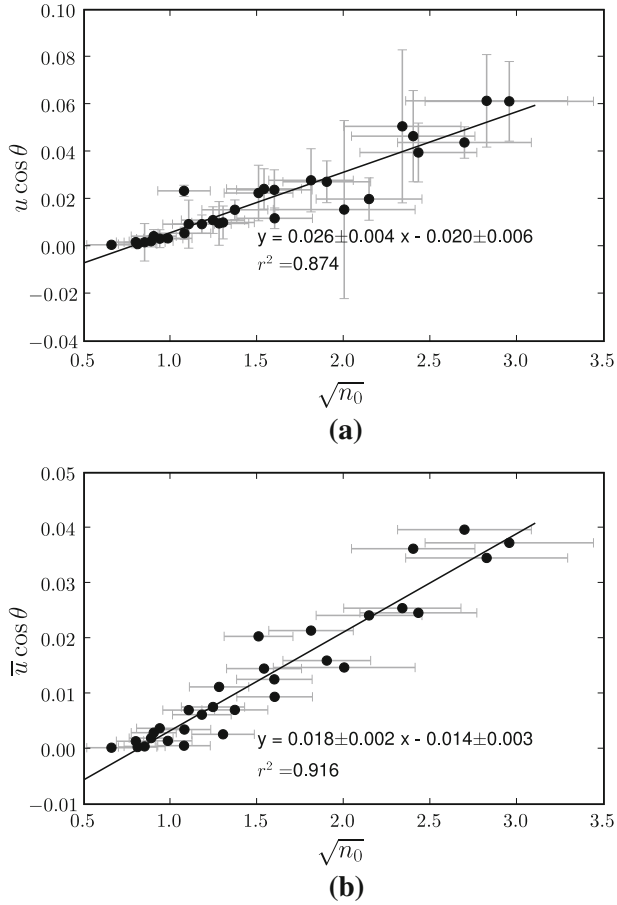

Fig. 21—A correlation between the local and average characteristic velocity with the cosine shape factor and the square root of depression depth. The error bars are ±1 standard deviation. (*a*) Local velocity and (*b*) average velocity.

when $u\cos\theta$ and $\overline{u}\cos\theta$ are plotted against the square root of the depression depth, linear relationships are revealed. At this stage, there no theoretical justification for this relationship, but it should be noted that the depression depth varies from 0.5 cm to 9 cm, so that this relationship holds over a length scale more than one order of magnitude in these experiments. Nevertheless, additional experimental and theoretical verification is necessary. The potential application of this finding is important. From the gas velocity, lance height, and cavity shape, one can calculate the local liquid velocities (for the calculation of mass transfer coefficients) and the bulk liquid velocities (for the calculation of mixing phenomena).

IV. CONCLUSIONS

From the current study, the following conclusions were drawn:

- The relation between surface depression depth and the supplied gas momentum was consistent with previous researchers[6] and was extended to higher flow rates.
- Molloy's[4] classification was reinterpreted with impact velocity at the dimpled surface depth.
- The critical cavity depth for the onset of splashing is approximately 1.2 cm, and it decreases with increasing lance height because the increased cavity width provides more contact for momentum transfer.
- Surface instability and the onset of splashing were interpreted with the Blowing number.
- To find characteristic oscillation frequencies, a fast Fourier transform technique was applied. The frequency varied between 2 and 12 Hz, but it was difficult to correlate the frequency to the jetting conditions.
- The power spectral density function was found useful to analyze the energy associated with variations in surface profile, cavity depth, cavity width, and the horizontal position of the cavity tip. The wave numbers of the distribution were shifted to a lower range when the cavity is in the penetration stage.
- The slopes of the power spectral density function against frequency generally show a slope of –5/3, and it is thought to be related to the attenuation of turbulent fluctuations around the impingement point.
- An energy transfer index was defined to characterize the transfer of kinetic energy from the gas jet to the liquid. The PIV measurements of liquid velocity were used to calculate the index. Beyond the dimpling regime, the index showed little dependency on the gas flow rate but increased as the lance height increased. The latter finding is attributable to the wider cavity at higher lance height, which gives the gas more opportunity to move the liquid.
- An analysis of the momentum transfer at the gas–liquid interface also shows that wider cavities increased the liquid velocity near the interface and the average recirculation velocity.
- A relationship between the cavity shape and momentum transfer is proposed.

APPENDIX

The PSD distribution is defined as

$$\text{PSD}\ (f) = \lim_{T\to\infty}\frac{1}{2T}\left[\int_{-T}^{T} X(t)e^{-i2\pi ft}dt\right]^2 \qquad [A1]$$

which is equivalent to the Fourier transform of an autocorrelation of $X(t)$

$$\text{PSD}\ (f) = \int_{-\infty}^{\infty}\lim_{T\to\infty}\frac{1}{2T}\left[\int_{-T}^{T} X(t)X(t+\tau)dt\right]e^{-i2\pi f\tau}d\tau \qquad [A2]$$

According to Priestley,[51] the PSD can be interpreted as "contribution to the total power of $X(t)$ by components with frequencies between f and $f + df$." This PSD is used widely for time series analysis and wave analysis, and it is mathematically equivalent to the energy density spectra of the spectral analysis of turbulence. The numerical implementations are well described in Otnes and Enochson.[52] A numerical library matplotlib (http://matplotlib.sourceforge.net/) of Python programming language was used for PSD computation; the Hanning windowing option was used to reduce numerical leakage, which is described in Otnes and Enochson.[52]

NOMENCLATURE

d_c	cavity width
d_t	cavity top lip width
d_0	nozzle diameter
g	gravity constant
h	distance from nozzle to initial surface
k	wave number
K	turbulent jet constant
$\dot{M}$	gas momentum rate
n_0	depression depth
Q	gas flow rate
x	distance from the nozzle exit
u_s	gas impact point velocity
u_0	gas nozzle exit velocity
u_m	turbulent jet centerline velocity
Re	Reynolds number $\left(=\frac{\rho uL}{\mu}\right)$
η	gas deflection coefficient, the ratio of tangential gas velocity to the jet velocity at the impingement point
λ	wavelength
ρ_l	liquid density
σ	surface tension

REFERENCES

1. H.W. Meyer, W.F. Porter, G.C. Smith, and J. Szekely: *J. Met.*, 1968, pp. 35–42.
2. D. Price: *Process Engineering of Pyrometallurgy*, London, UK, 1974, pp. 8–15.
3. K.D. Peaslee and D.G.C. Robertson: *Steelmaking Conf. Proc.*, 1994, vol. 77, pp. 713–22.
4. N.A. Molloy: *J. Iron Steel Inst.*, 1970, pp. 943–50.

5. R.B. Banks and D.V. Chandrasekhara: *J. Fluid Mech.*, 1963, vol. 15, pp. 13–34.
6. N. Rajaratnam: *Turbulent Jets*, Elsevier, Atlanta, GA, 1976.
7. E.T. Turkdogan: *Chem. Eng. Sci.*, 1966, vol. 21, pp. 1133–44.
8. S.C. Koria and K.W. Lange: *Steel Res.*, 1987, vol. 58 (9), pp. 421–26.
9. F. Qian, R. Mutharasan, and B. Farouk: *Metall. Mater. Trans. B*, 1996, vol. 27B, pp. 911–20.
10. A. Nordquist, N. Kumbhat, L. Jonsson, and P. Jönsson: *Steel Res. Int.*, 2006, vol. 77 (2), pp. 82–90.
11. F.R. Cheslak, J.A. Nicholls, and M. Sichel: *J. Fluid Mech.*, 1969, vol. 36, pp. 55–62.
12. R.C. Urquhart and W.G. Davenport: *Can. Metall. Q.*, 1973, vol. 12 (4), pp. 507–16.
13. K.D. Peaslee and D.G.C. Robertson: *Electric Furnace Conf. Proc.*, 1993, pp. 403–11.
14. K.D. Peaslee and D.G.C. Robertson: *Steelmaking Conf. Proc.*, 1995, pp. 689–96.
15. N. Standish and Q. He: *ISIJ Int.*, 1989, vol. 29 (6), pp. 455–61.
16. A. Chatterjee and A.V. Bradshaw: *J. Iron Steel Inst.*, 1972, pp. 179–87.
17. Q. He and N. Standish: *ISIJ Int.*, 1990, vol. 30 (4), pp. 305 09.
18. Subagyo, G. Brooks, K. Coley, and G.A. Irons: *ISIJ Int.*, 2003, vol. 43 (7), pp. 983–89.
19. R. Li and R.L. Harris: *Pyrometallurgy 95 Conf. Proc.*, 1995, London, UK, pp. 107–24.
20. S. Chandrasekhar: *Hydrodynamic and Hydromagnetic Stability*, Dover Publication Inc., New York, NY, 1961.
21. T. Funda and D.D. Joseph: *J. Fluid Mech.*, 2001, vol. 445, pp. 263–83.
22. W.G. Davenport, D.H. Wakelin, and A.V. Bradshaw: *Heat and Mass Transfer in Process Metallurgy*, 1967, London, UK, pp. 207–45.
23. F.M. White: *Fluid Mechanics*, 6th ed., McGraw-Hill, New York, NY, 2008, p. 348.
24. I. Wygnanski and H. Fiedler: *J. Fluid Mech.*, 1969, vol. 38, pp. 577–612.
25. M. Gharib and D. Daribi: *Flow Visualization*, World Science Publishing Co., Hackensack, NJ, 2000, pp. 123–47.
26. A.K. Prasad: *Current Sci.*, 2000, vol. 79 (1), pp. 51–60.
27. R.D. Kean and R.J. Adriantems: *Meas. Sci. Technol.*, 1990, vol. 1, pp. 1202–15.
28. J. Kitscha and G. Kocamustafaogullari: *Int. J. Multiphase Flow*, 1989, vol. 15 (4), pp. 573–88.
29. J.M. Elson and J.M. Bennet: *Applied Optics*, 1995, vol. 34 (1), pp. 201–08.
30. D.D. Joseph, J. Belanger, and G.S. Beavers: *Int. J. Multiphase Flow*, 1999, vol. 25, pp. 1263–1303.
31. M. Lee, V. Whitney, and N. Molloy: *Scand. J. Metall.*, 2001, vol. 30, pp. 330–36.
32. M.S. Lee, S.L. O'Rourke, and N.A. Molloy: *Scand. J. Metall.*, 2003, vol. 32, pp. 281–88.
33. B. Metcalf, J. Longo, S. Ghosh, and F. Stern: *J. Fluid Structures*, 2006, vol. 22, pp. 77–98.
34. G.A. Zarruk: *Meas. Sci. Technol.*, 2005, vol. 16, pp. 1970–75.
35. H. Mitsuyasu and T. Honda: *J. Fluid Mech.*, 1982, vol. 123, pp. 425–42.
36. M. Lommer and M.T. Levinson: *J. Fluorescence*, 2002, vol. 12, pp. 45–50.
37. V.E. Zakharov, G. Falkovich, and V.S. Lvov: *Kolmogorov Spectra of Turbulence I*, Springer-Verlag, New York, NY, 1992.
38. E. Falcon, C. Laroche, and S. Fauve: *Phys. Rev. Lett.*, 2007, vol. 98, p. 094503.
39. D. Dabiri: *J. Fluid Mech.*, 2003, vol. 480, pp. 217–32.
40. W.K. George, P.D. Beuther, and R.E. Arndt: *J. Fluid Mech.*, 1984, vol. 148, pp. 155–91.
41. R.A. Handler, T.F. Swean, Jr., R.I. Leighton, and J.D. Swaringen: *AIAA J.*, 1993, vol. 31 (11), pp. 1998–2007.
42. M. Fulgosi, D. Lakehal, D. Banerjee, and V. De Angelis: *J. Fluid Mech.*, 2003, vol. 482, pp. 319–45.
43. B.H. Brumley and G.H. Jirka: *J. Fluid Mech.*, 1987, vol. 183, pp. 235–63.
44. Y. Guo and D.H. Wood: *Exp. Therm. Fluid Sci.*, 2002, vol. 25, pp. 605–14.
45. N. Rajaratnam and B.S. Pani: *ASCE J. Hydraulic Division*, 1974, vol. 100(HY1), pp. 69–83.
46. G. Padmanabham and B.H.L. Gowda: *Trans. ASME J. Fluid Eng.*, 1991, vol. 113, pp. 620–28.
47. A.W.-K. Law and Herlina: *J. Hydraul. Eng.*, 2002, vol. 128 (2), pp. 161–74.
48. J. Szekely and N.J. Themelis: *Rate Phenomena in Process Metallurgy*, Wiley, New York, NY, 1971.
49. K. Nakanishi, K. Saito, T. Nozaki, Y. Kato, K. Suzuki, and T. Emi: *Steelmaking Conf.*, 1982, pp. 101–08.
50. K.C. Mills, Y. Su, A.B. Fox, Z. Li, R.P. Thackray, and H.T. Tsai: *ISIJ Int*, 2005, vol. 45 (5), pp. 619–33.
51. M.B. Priestley: *Spectral Analysis and Time Series*, vol. 1: Univariate Series, Volume 1 of Probability and Mathematical Statistics, Academic Press, Atlanta, GA, 1981.
52. S. Otnes and L. Enochson: *Digital Time Series Analysis*, Wiley, New York, NY, 1972.